Tracking Hg2+ adsorption by reduced graphene oxide in continuous flow by in situ techniques

Downloaded from: https://research.chalmers.se, 2025-10-16 17:31 UTC

Citation for the original published paper (version of record):

Andrade, M., Bugaev, A., Skorynina, A. et al (2025). Tracking Hg2+ adsorption by reduced graphene oxide in continuous flow by in situ techniques. Journal of Environmental Chemical Engineering, 13(5). http://dx.doi.org/10.1016/j.jece.2025.118680

N.B. When citing this work, cite the original published paper.

research.chalmers.se offers the possibility of retrieving research publications produced at Chalmers University of Technology. It covers all kind of research output: articles, dissertations, conference papers, reports etc. since 2004. research.chalmers.se is administrated and maintained by Chalmers Library

(article starts on next page)

Journal of Environmental Chemical Engineering 13 (2025) 118680

Contents lists available at ScienceDirect

Journal of Environmental Chemical Engineering

journal homepage: www.elsevier.com/locate/jece

Tracking Hg^{2+} adsorption by reduced graphene oxide in continuous flow by *in situ* techniques

Marcelo A. Andrade [a,b,c], Aram L. Bugaev [d], Alina Skorynina [e], Camille Douard [a,b], Olivier Crosnier [a,b], Björn Wickman [f], Patrik Johansson [c,f], Thierry Brousse [a,b,*]

[a] Nantes Université, CNRS, Institut des Matériaux de Nantes Jean Rouxel, IMN. 2 Rue de la Houssinière, Nantes, France
[b] Réseau sur le Stockage Electrochimique de l'Energie (RS2E), FR CNRS 3459, Hub de l'Energie,, 15 Rue Baudelocque, Amiens 80039, France
[c] Alistore-ERI European Research Institute, FR CNRS 3104, Hub de l'Energie, 15 Rue Baudelocque, Amiens 80039, France
[d] Center for Photon Science, Paul Scherrer Institut, Forschungsstrasse 111,, Villigen 5232, Switzerland
[e] ALBA Synchrotron, Cerdanyola del Valles, Barcelona 08290, Spain
[f] Department of Physics, Chalmers University of Technology, Gothenburg SE-412 96, Sweden

ARTICLE INFO

Keywords:
Absorbent
Reduced graphene oxide
Mercury removal
Waste water treatment
Electrochemical quartz crystal Microbalance
X-ray absorption spectroscopy

ABSTRACT

Mercury pollution poses severe risks to environmental and public health due to its high toxicity and persistence. The use of physical adsorbents for heavy metal cation uptake is a straightforward solution for many applications, but a better fundamental understanding of the mechanism is crucial for rational improvement. We have investigated the adsorption of mercury ions on reduced graphene oxide (rGO) in real time by coupling continuous flow setups with *in situ* analytical techniques: X-ray absorption spectroscopy (XAS) and electrochemical quartz crystal microbalance with dissipation monitoring (EQCM-D). The microfluidic setup provided a practical and efficient platform for mimicking realistic conditions, requiring minimal sample volumes and enabling continuous flow analysis, while the *in situ* XAS brought detailed atomic and electronic structural information, allowing for following changes in mercury ion coordination as adsorption proceeded. Similarly, EQCM-D followed the mass changes and viscoelastic properties of the rGO layer under dynamic flow conditions upon adsorption. The approach distinguished chemisorbed from physisorbed mercury cations, revealing a yet undescribed transition between the two forms. This enables a better understanding of the adsorption mechanisms and highlights the benefits of coupling microfluidic systems with advanced *in situ* techniques.

1. Introduction

Mercury pollution is a significant environmental and public health concern due to its high toxicity and persistence in various ecosystems [1]. Among the various methods for mercury decontamination, adsorption stands out for its simplicity, efficiency, and cost-effectiveness [2]. A better understanding of the adsorption mechanisms at the molecular level is essential for rational optimization of adsorbent materials and improved performance.

Liu et al. [3] studied the removal of Hg^{2+} cations by carbonaceous materials using biochars derived from 36 feedstocks processed at different pyrolysis temperatures. They attributed mercury binding to interactions with functional groups, as confirmed by X-ray absorption near edge structure (XANES) and extended X-ray absorption fine structure (EXAFS) analyses, with a preference for sulfur-rich sites. However, the same study highlights the environmental concerns related to sulfur-containing biochars, which could promote mercury methylation via sulfate-reducing bacteria. These findings show the importance of material selection and their potential secondary environmental impact, while still being limited in replicating the dynamic conditions of real-world systems by using batch experiments.

Reduced graphene oxide (rGO) has emerged as a promising sulfur-free adsorbent for heavy metals, particularly mercury, due to its high surface area, richness in functional groups, and large availability [4]. Barra et al. [5] explored the use of chemically modified rGO for the efficient adsorption and secure immobilization of Hg^{2+} from water. They introduced modifications with caffeic acid and chitosan to enhance sorption efficiency and structural integrity, achieving a high degree of reduction and porosity which facilitated Hg removal under realistic contamination scenarios. The materials demonstrated low desorption

* Corresponding author at: Nantes Université, CNRS, Institut des Matériaux de Nantes Jean Rouxel, IMN. 2 Rue de la Houssinière, Nantes, France.
E-mail address: thierry.brousse@univ-nantes.fr (T. Brousse).

https://doi.org/10.1016/j.jece.2025.118680
Received 27 April 2025; Received in revised form 11 August 2025; Accepted 12 August 2025
Available online 14 August 2025
2213-3437/© 2025 The Author(s). Published by Elsevier Ltd. This is an open access article under the CC BY license (http://creativecommons.org/licenses/by/4.0/).

rates, enabling safe storage of adsorbed Hg in solid waste form [5]. In our recent work, rGO was synthesized via a straightforward hydrothermal method, and its capacity to preferentially adsorb Hg^{2+} ions was demonstrated up to 240 mg of Hg^{2+} ions per gram of adsorbent at room temperature [6]. Furthermore, the spent adsorbent was then directly recycled into electrodes for energy storage, giving it a second life before becoming waste, which remediates even further any potential secondary impacts by the generated solid waste.

To further enhance the understanding of adsorption mechanisms, it is crucial to investigate not only the capacity of materials like rGO, but also the processes occurring during adsorption. Microfluidic systems offer a practical and powerful platform for characterization under continuous flow [7–10]. Over the past three decades, microfluidics has transformed from its origins in microelectronics into a multidisciplinary field with significant applications in biology, chemistry, and engineering. Recent advancements have enabled applications such as high-throughput chemical analysis that presents an interdisciplinary solution with systems that are simple to use, require minimal sample volumes, and can mimic realistic conditions [11]. By integrating microfluidic devices with *in situ* analytical methods, such as X-ray absorption spectroscopy (XAS) [7,8] and electrochemical quartz crystal microbalance with dissipation monitoring (EQCM-D), we investigate herein in real time the adsorption of Hg^{2+} ions on rGO.

2. Results and discussion

2.1. Materials characterization

Reduced graphene oxide (rGO) foam was used as an adsorbent, and its full characterization was reported recently [6]. In brief, the rGO foam was analyzed using scanning electron microscopy (SEM), which revealed a highly porous, branched morphology with exposed graphene edges, as also confirmed by transmission electron microscopy (TEM). The 3D structure was formed after the hydrothermal reduction of graphene oxide (GO), leading to a self-standing rGO foam. Gas adsorption experiments showed that the rGO foam had a specific surface area (SSA) of up to 214 $m^2 \cdot g^{-1}$ with an average pore size of 5.4 nm. X-ray photoelectron spectroscopy (XPS) confirmed the reduction of GO to rGO with a 24 % decrease in oxygen content, supported by energy-dispersive spectroscopy (EDS) and electron energy loss spectroscopy (EELS).

The Fourier-transform infrared (FTIR) spectrum of rGO showed a reduction in the intensity of carboxyl (—COOH) and hydroxyl (—OH) group vibrations peaks as compared to GO. The appearance of a peak at 1570 cm^{-1} corresponding to aromatic C═C stretching modes indicated the restoration of the sp^2-hybridized carbon network. In addition, the Raman spectrum exhibited the characteristic D and G bands of graphene-based materials, associated with lattice defects and disorder, and to the in-plane vibration of sp^2 carbon atoms, respectively. The intensity ratio of D to G bands (I_D/I_G) was slightly reduced in rGO as compared to GO, suggesting a decrease in defect density and an increase in the graphitic nature of the material. The presence of defects was, however, still evident, which can be beneficial for the material's functionality as an adsorbent. Thermogravimetric analysis (TGA) under air revealed that rGO exhibited stability up to 600 °C, after which total oxidation occurred, while GO had *ca.* 50 % weight loss already at 300 °C.

2.2. Bulk adsorption

2.2.1. Langmuir and Freundlich model fits to isotherm

To characterize the equilibrium interaction properties of rGO with Hg^{2+} cations, batch adsorption experiments were conducted at 298 K, whereas the adsorption isotherm can help to elucidate the nature of the adsorption sites and the mechanisms involved, using the adsorption capacity (q_e / mg·g^{-1}) as a function of the equilibrium concentration (C_e / mg·L^{-1}) of the adsorbate (Fig. 1) [12].

Using these data, the adsorption capacity was calculated as:

$$q_t = \frac{C_0 - C_t}{d} \quad (1)$$

where q_t (mg·L^{-1}) is the time-dependent adsorption capacity (and $q_t = q_e$ when equilibrium is achieved), C_0 is the initial concentration of adsorbate, C_t (mg·L^{-1}) is the time-dependent solution concentration (and $C_t = C_e$ at equilibrium), and d (g·L^{-1}) is the dose of adsorbent applied (*i.e.* adsorbent mass divided by the adsorbate solution volume). The experimental data was then fit using Langmuir and Freundlich's models based on the following equations:

$$q_e = \frac{q_{max} K_L C_e}{1 + K_L C_e} \quad (2)$$

$$q_e = K_F C_e^{\frac{1}{n}} \quad (3)$$

whereby the equilibrium adsorption capacity (q_e) is correlated with the equilibrium concentration (C_e) by providing intrinsically dependent

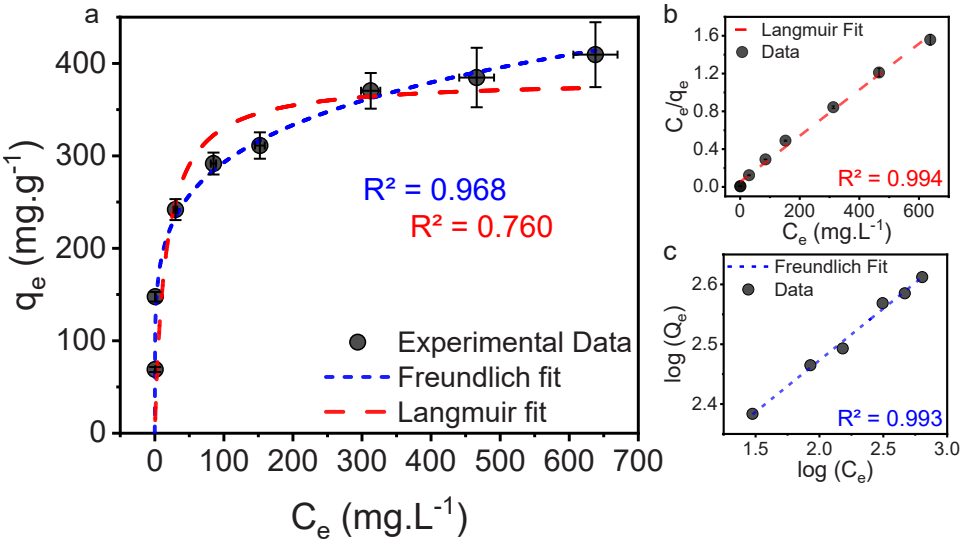

Fig. 1. Adsorption isotherm at 298 K using a dose of rGO of d = 0.5 g·L^{-1} and initial concentrations ranging from C_0 = 50 mg·L^{-1} to 1000 mg·L^{-1} at pH = 3. a) The dashed curves are the non-linear fitting of Freundlich (blue) and Langmuir (red) models; b) Linear fit of Langmuir model; c) Linear fit of Freundlich model.

parameters. The Langmuir model in Eq. 2 uses the maximum adsorption capacity (q_{max}) and the Langmuir equilibrium constant (K_L / $L{\cdot}g^{-1}$), related to adsorption energy, while Eq. 3 introduces the Freundlich constant (K_F / $(mg{\cdot}g^{-1}){\cdot}(L{\cdot}mg^{-1})^{1/n}$), related to the adsorption capacity, and the heterogeneity factor *n*, which gives insights on adsorption preferences. Finally, the linearization of Eqs. 2 and 3 allows the following expressions (Figs. 1b and 1c), respectively:

$$\frac{C_e}{q_e} = \frac{1}{q_{max}K_L} + \frac{C_e}{q_{max}} \tag{4}$$

$$\log(q_e) = \log(K_F) + \frac{1}{n}\log(C_e) \tag{5}$$

Upon linearization, the two models fit very well the experimental data, with a correlation coefficient (R^2-score) > 0.99 in both cases. Generally, the fitting using the non-linearized equations provides a more mathematically straightforward comparison between the different models [13]. A summary of the parameters calculated using Eqs. 2 to 5 is presented in Table 1.

The linearized models do not directly indicate the best fit for the system, but parameter similarity between linear and non-linear fittings suggests a good correlation with the underlying physical phenomena. The Freundlich model fits the data better ($R^2 > 0.99$), which reflects the heterogeneous surface of rGO, unlike the Langmuir model, which assumes a homogeneous monolayer adsorption. The Langmuir model's high q_{max} (410 ± 13 $mg{\cdot}g^{-1}$) highlights the strong rGO-Hg^{2+} interactions, but its low K_L (< 0.1 $L{\cdot}g^{-1}$) suggests weak physisorption in the non-functionalized regions of rGO, and its poor non-linear fit in fact limits the model's applicability.

On the other hand, the Freundlich model describes well the system's heterogeneity, with K_F indicating high affinity and 1/n (~0.2) showing strong deviation from Langmuir's linearity, in particular for higher values of C_0. This describes a heterogeneous surface with the presence of sites strongly interacting with the Hg^{2+} cations, which thus are responsible for the high uptake capacity of mercury, in particular at lower concentrations, and also regions of lower affinity to the Hg^{2+} cations, possibly mainly related to physisorption, with increasing q_e as C_0 increases.

2.2.2. Adsorption kinetics

The kinetics of adsorption was studied in a batch experiment to better understand the nature of the interactions between the rGO surface and the Hg^{2+} cations as a function of time (Fig. 2).

To fit the experimental data and describe the rGO-Hg system, the most common methods are the pseudo-first order, pseudo-second order, and Elovich models, described by Eqs. 6, 7 and 8, respectively [13]:

$$q_t = q_e(1 - e^{-k_1 t}) \tag{6}$$

$$q_t = \frac{k_2 q_e^2 t}{1 + k_2 q_e t} \tag{7}$$

$$q_t = \frac{1}{\beta}\ln t + \frac{1}{\beta}\ln\alpha\beta \tag{8}$$

Here, the adsorption rate constants for the pseudo-first and second order models are presented as k_1 (s^{-1}) and k_2 ($g{\cdot}mg^{-1}{\cdot}s^{-1}$), respectively, while the Elovich model introduces the α ($mg{\cdot}g^{-1}s^{-1}$) and β ($g{\cdot}mg^{-1}$) parameters, related to the initial sorption rate and to the influence of surface coverage and the activation energy of the chemisorption process, respectively. The linear fitting of these models was also considered and calculated using Eqs. 9–11:

$$\ln\left(1 - \frac{q_t}{q_e}\right) = -k_1 t \tag{9}$$

$$\frac{t}{q_t} = \frac{1}{k_2 q_e^2} + \frac{t}{q_e} \tag{10}$$

$$\ln q_t = \ln\frac{1}{\alpha} + [\ln(1 + \alpha\beta t)]^2 \tag{11}$$

The pseudo-first order model assumes non-reversible adsorption on localized sites without interactions between sorbed ions, with a constant adsorption energy, and a monolayer forming at saturation. In contrast, the pseudo-second order model assumes a similar localized adsorption process but with kinetics governed by a second-order rate equation, reflecting a greater dependency on site availability. The Elovich model, however, introduces interactions between sorbed ions and considers the adsorption energy to increase linearly as a function of surface coverage. This thus accounts for more complex adsorption dynamics, including negligible initial uptake and an exponential phase, making it more versatile for heterogeneous systems as compared to the simplified assumptions of the pseudo-first and second-order models [13]. A summary of the calculated kinetics parameters and the constants can be found in Table 2.

The fast sorption kinetics (Fig. 2a) enables equilibrium after only 20 min of contact with the adsorbent. The maximum adsorption capacity of 293 $mg{\cdot}g^{-1}$ at 60 min of adsorption is a relatively high value for Hg^{2+} and agrees with the isotherm experiments. For both the non-linearized pseudo-first and pseudo-second order models, the calculated q_e are very similar to the experimental, and especially the latter fit well with an $R^2 > 0.92$. The pseudo-first order model fit fails at the beginning of the adsorption data. The adsorbate is rapidly trapped for the first 5 min, followed by slower adsorption from 5 to 15 min, and finally, equilibrium is reached. This behavior is more accurately described by the pseudo-second order model, as the availability of sites is taken into account. The Elovich model provides the best non-linear fit and exhibits a good linear correlation. It describes well the three zones in time, evidencing two distinct types of sorption that could occur at different sites. Different models can take into account diffusion-limiting steps of sorbate from solution to the adsorbent bulk, as well as intra-particular diffusion, confirming that more than one mechanism is governing this adsorption process (Figure S1).

2.3. Microfluidic adsorption

2.3.1. Local structure around the mercury cations

The adsorption of Hg^{2+} cations by rGO was followed in real-time by *in situ* XAS measurements by tracking the changes in the mercury signal above the Hg L_3-edge (Fig. 3a).

The XANES and EXAFS spectra measured for a water solution (dashed black lines in Fig. 3a,b) are characteristic of Hg^{2+} coordinated with six water molecules, in agreement with previously reported data [14]. Immediately after the beginning of adsorption in rGO, a decrease in the first coordination shell occurs (from dashed black to solid blue in

Table 1
Adsorption isotherm calculated parameters.

	Model	K_L ($L{\cdot}g^{-1}$)	q_{max} ($mg{\cdot}g^{-1}$)	K_F ($(mg{\cdot}g^{-1}){\cdot}(L{\cdot}mg^{-1})^{1/n}$)	n	R^2
Non-linearized	Langmuir	0.06 ± 0.05	383 ± 40	-	-	0.760
	Freundlich	-	-	124 ± 13	5.3 ± 0.5	0.968
Linearized	Langmuir	0.05 ± 0.02	410 ± 13	-	-	0.994
	Freundlich	-	-	134 ± 5	5.8 ± 0.3	0.993

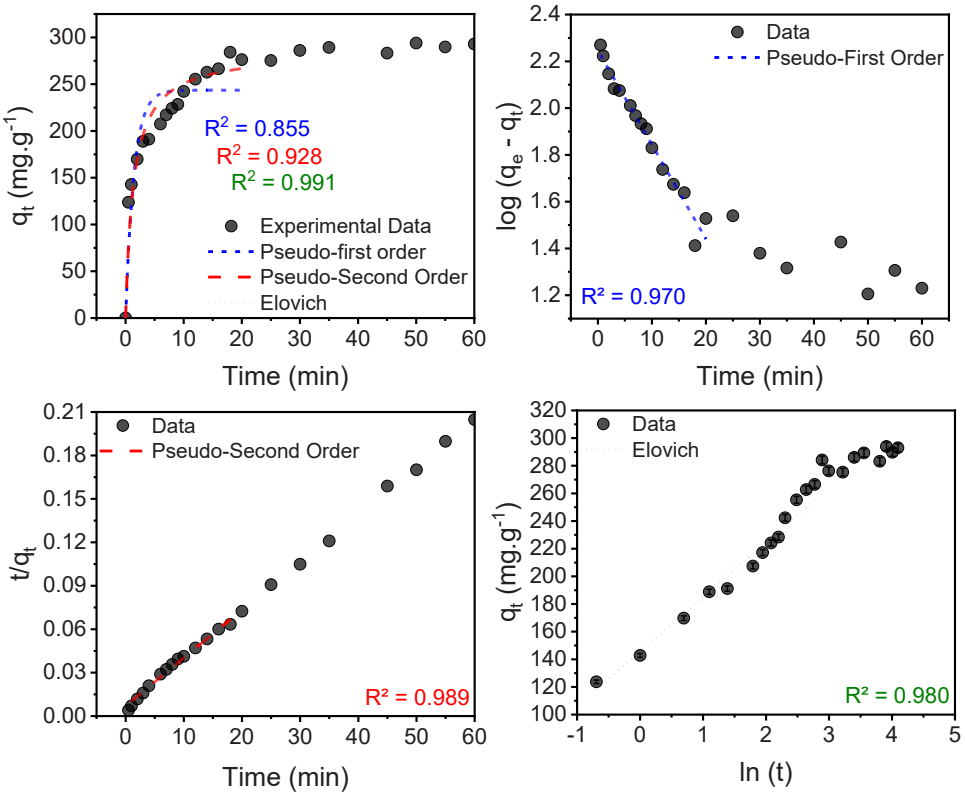

Fig. 2. Bulk adsorption kinetics at 298 K with a dose of rGO of d = 0.5 g·L^{-1}, C_0 = 300 mg·L^{-1} and pH = 3. a) Non-linear fitting of pseudo-first order (blue), Pseudo-second order (red) and Elovich (green) models before reaching equilibrium conditions; b), c) and d) are the linear fitting of the same models, respectively.

Table 2
Calculated kinetics parameters.

	Model	q_e (mg·g^{-1})	Constant 1	Constant 2	R^2
	Experimental	293			
Non-linearized	Pseudo-first order	280 ± 9	$K_1 = 68 \pm 9 \times 10^{-2}$ min^{-1}	-	0.855
	Pseudo-second order	285 ± 5	$K_2 = 25 \pm 3 \times 10^{-4}$ g·mg^{-1}·min^{-1}	-	0.928
	Elovich	-	$\alpha = 11 \pm 2 \times 10^{2}$ mg·g^{-1}·min^{-1}	$\beta = 23 \pm 1 \times 10^{-3}$ g·mg^{-1}	0.991
Linearized	Pseudo-first order	178 ± 9	$K_1 = 9.3 \pm 0.4 \times 10^{-2}$ min^{-1}	-	0.970
	Pseudo-second order	296 ± 8	$K_2 = 14 \pm 2 \times 10^{-4}$ g·mg^{-1}·min^{-1}	-	0.989
	Elovich	-	$\alpha = 16 \pm 1 \times 10^{2}$ mg·g^{-1}·min^{-1}	$\beta = 25 \pm 1 \times 10^{-3}$ g·mg^{-1}	0.980

Fig. 3b). The fitting of the blue spectrum gives the coordination number of 1.6 ± 0.6 and interatomic distance of 2.11 ± 0.03 Å, corresponding to C neighbours (C/N/O are indistinguishable by EXAFS). The total mercury loading per volume of sample (internal sampled volume of the tube, in cm^3) was also calculated based on the edge jump at Hg L_3-edge (grey line, Fig. 3c). The maximum loading was reached after 40 min, as a result of the accumulation of Hg^{2+} cations in the rGO due to adsorption. After this plateau, the total mercury loading slightly decreases as more solution keeps flowing, indicating the possible attainment of a saturation equilibrium. This behavior implies that as adsorption sites become increasingly occupied over time, new chemical environments around the mercury ions form. This has a direct correlation to the thermodynamic and kinetic descriptions of the system, which would first promote the interactions between the Hg^{2+} cations to the rGO functional groups (Fig. 3b). During the sorption process, the speciation of Hg changes, which is evidenced by both XANES and EXAFS spectra (Figs. 3a, 3b, from blue to red). In XANES region, the increase in the pre-edge is accompanied with a flattening of the resonance after the edge responsible for the transition of electron to the unoccupied molecular *d*-orbitals, while in EXAFS, the decrease of the Hg—C contribution is observed (in the region from 1 to 2 Å, phase-uncorrected), both indicating a weakly coordinated Hg^{2+}-species [14]. Both facts indicate that most Hg-species in the sample represented by the red spectra are indeed physisorbed and not chemisorbed.

Fig. 3c also shows the mercury loading of each species, red and blue, as a function of adsorption time. Initially, blue species increase rapidly in concentration, up to its maximum at around 30 min, and gradually decrease after that. The red species start appearing slowly after t = 10 min and gradually take over the main contribution as the blue species decreases after 30 min, reaching a plateau of around 12 mg·cm^{-3} after 60 min. If we attribute the red species to physisorbed Hg^{2+} cations, it is reasonable to think that, as a less favorable process, it was competing with the blue species in the beginning, when it finally increased in significance and reached saturation as all the available rGO sites were occupied. On the other hand, in the case of the blue species, its contribution to the spectra decreases continuously after *ca.* 30 min.

This new phenomenon can tentatively be explained by the substitution of the already adsorbed Hg^{2+} cations by incoming H_3O^+ from the flowing solution. It is also reasonable to assume that the physisorbed species, less strongly bound to the solid, are washed away by DI water when recovering the filtered solid residue, leading to a spectrum of the dried rGO/Hg_{ads} being more similar to the adsorption beginning (blue)

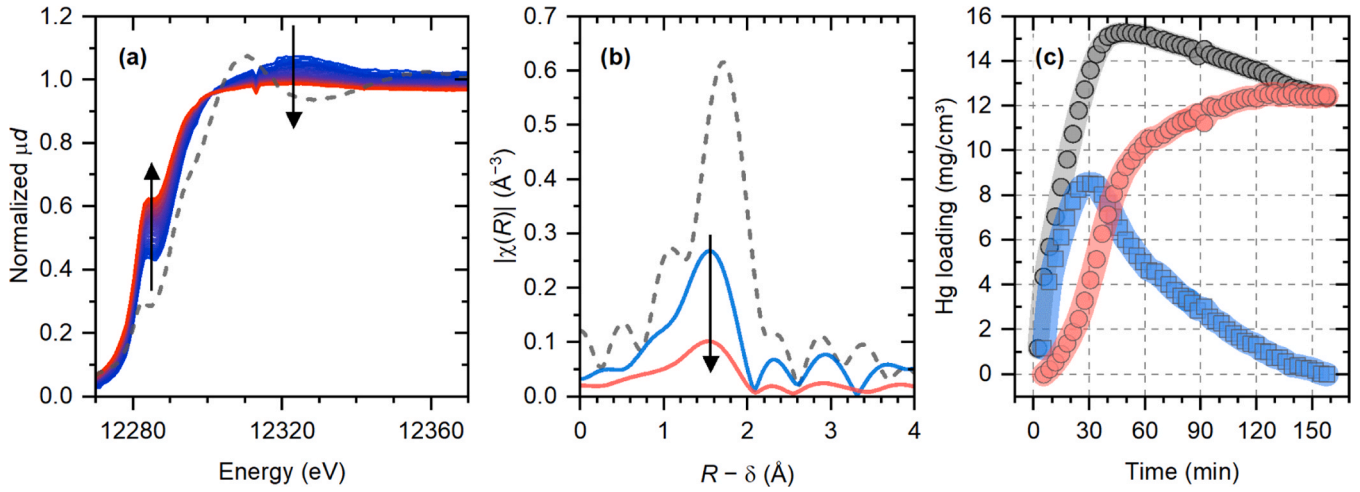

Fig. 3. a) Evolution of mercury L_3-edge XANES spectra with time (from blue to red) upon cations adsorption, with the spectrum of $Hg(NO_3)_2$ solution shown in dashed grey. b) FT-EXAFS spectra of the first (blue) and an average of the last 10 spectra (red) collected during sorption with the spectrum of $Hg(NO_3)_2$ solution (dashed grey). c) Concentration profiles of mercury species per volume of capillary as a function of adsorption time, calculated based on the jump at Hg L_3-edge. Total mercury loading is shown in grey, and its components are the red and blue lines relative to two different Hg species, whose spectra are shown in (a) (blue, related to the early stage of adsorption, and red, predominantly to its end after 150 min).

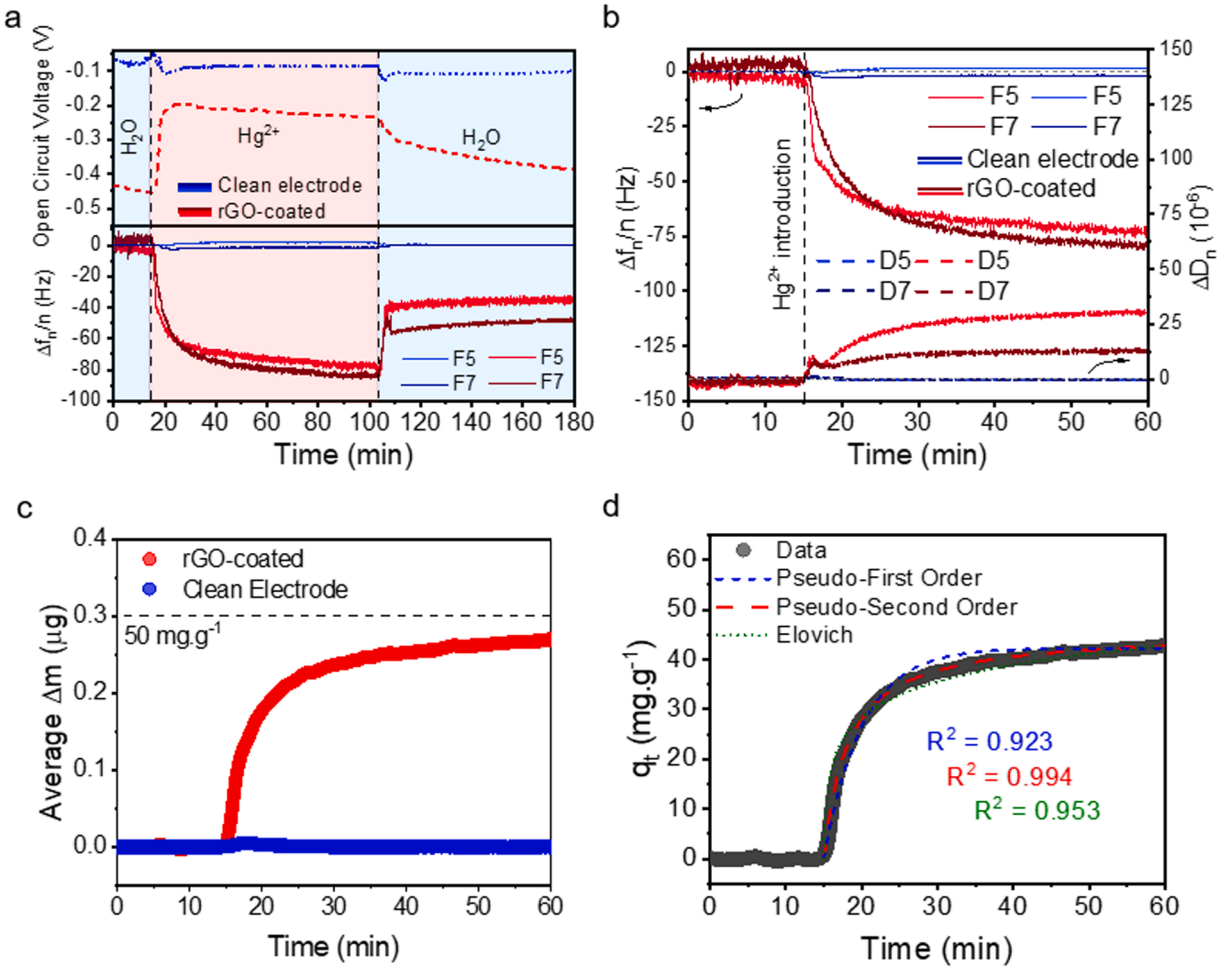

Fig. 4. a) Flow adsorption experiment showing the OCV on top, alongside with the QCM-D 5th (lighter line tonalities) and 7th (dark line tonalities) harmonic frequencies variations at the bottom. Water flows from t = 0 min until t = 15 min, when Hg^{2+} cations arrive at the quartz electrode with rGO (red) and without (blue). After t = 100 min the mercury solution is switched back to DI water; b) Normalized frequency (solid line) and dissipation (dashed) variations of the rGO-coated (red lines) and bare (blue lines) electrodes. c) Estimated mass variation of the rGO-coated (red) and bare (blue) electrodes from averaging normalized 5th and 7th harmonic variations. d) Non-linear fitting of pseudo-first order (blue) pseudo-second order (red) and Elovich (green) adsorption kinetics models to the estimated adsorption capacity vs. time. (For interpretation of the references to color in this figure legend, the reader is referred to the web version of this article.)

(Figure S2). Furthermore, in bulk adsorption, it is clear that Hg^{2+} exchanges for H_3O^+ from the rGO, as the pH of the solution decreases constantly as the adsorption takes place (Figure S3). To give further support to this assumption, Figure S4 demonstrates that the Hg^{2+} cations remain heterogeneously distributed at the rGO surface, preferably at smaller adsorbent particles rather than at big flat surfaces, which corroborates the hypothesis of washing out Hg^{2+} cations by the incoming solution.

2.3.2. Electrochemical quartz crystal microbalance with dissipation monitoring (EQCM-D)

The adsorption of Hg^{2+} cations from a 50 mg·L^{-1} solution was monitored under flow conditions using rGO deposited onto a carbon-coated electrode on an EQCM-D quartz crystal. The variations in frequency and dissipation were tracked alongside the open circuit voltage (OCV), highlighting the fast adsorption of Hg^{2+} ions by a thin drop-casted layer of rGO, as illustrated in Fig. 4.

Initially, both electrodes are exposed to water (t = 0–15 min), showing stable frequency and dissipation values. Upon introduction of Hg^{2+} cations at t = 15 min, a decrease in frequency and an increase in dissipation are observed for the rGO-coated electrode, indicating a significant mass increase. This effect is absent in the clean electrode, which serves as a baseline for the influences caused by the change in the flowing solution (ionic force, pH, viscosity, etc). The electrode's OCV varied as the solution changed from water to mercury nitrate, as a result of both the ionic force increase, as evidenced by the reversible OCV change on the clean electrode, as well as by the interaction of the cations to the surface, as evidenced by the irreversible OCV change in the rGO-coated electrode.

Frequency changes are observed in both electrodes when the flowing solution changes, regardless of adsorption. However, on the clean electrode surface, the frequency and dissipation changes are minimal and reversible, indicating no significant mass adsorption or structural changes. The introduction of Hg^{2+} to the rGO-coated electrode, on the other hand, results in significant, irreversible decreases in frequency and increases in dissipation, which do not revert to baseline levels upon subsequent water washes. The small decrease could be due to the removal of weakly physisorbed Hg^{2+} cations, which indicates a majority of strong and irreversible adsorption of Hg^{2+} ions onto the rGO layer.

The mass variation was estimated from the average changes in the 5th and 7th harmonics, chosen for their stability and consistency during the experiments (Fig. 4b), using the Sauerbrey equation:

$$\Delta m = -A\frac{\sqrt{\rho_q \mu_q}}{2{f_0}^2}\frac{\Delta f}{n} \quad (12)$$

Here, the mass variation Δm (g) in the piezoelectrically active crystal area A (cm^2) is directly related to the variation in frequency Δf (Hz) normalized by the overtone number $n = 1, 3, 5\ldots$ using a correlation constant that considers the fundamental frequency of the quartz, f_0 (Hz), its specific density ρ_q (g·cm^3) and its shear modulus μ_q (g·cm^{-1}·s^{-1}). The mass variation for the rGO-coated electrode increases rapidly upon Hg^{2+} introduction, reaching a plateau at around 0.26 μg, indicating the saturation of the adsorbent (Fig. 4c). Given the deposited rGO mass of approximately 6 μg (30 μg·cm^{-2}), this qualitatively represents an adsorption capacity of *ca.* 50 mg·g^{-1}, which is in agreement with the literature for this material [4,6]. In contrast, the clean electrode shows negligible mass change throughout the experiment, reinforcing that the observed mass increase is due to the rGO coating and not due to nonspecific phenomena on the base electrode.

The same models as applied above to the adsorption kinetics data were used to try to describe the adsorption phenomena as tracked by the EQCM-D (Fig. 4d). All three adsorption kinetic models fit the experimental data very well ($R^2 > 0.97$), but the pseudo-second order model fits particularly well, which could indicate a higher sensitivity of EQCM-D to the sites' energy increase with occupation. This fact also correlates with the rapid initial occupation of chemisorption sites presented in Fig. 3c, followed by a preferred physisorption as the sites become protonated, and a plateau in Hg loading, indicated by the mass increase.

3. Experimental

3.1. Synthesis procedures

Synthesis of graphene oxide (GO). GO was synthesized from graphite powder via an improved Hummer's method, following the procedure outlined in a previous publication [6]. In brief, graphite was oxidized in a sulfuric and phosphoric acid mixture with potassium permanganate as the oxidizing agent. The mixture was stirred at 50 °C for 3 h and then at room temperature for 3 days. The resulting solution was added with DI water and 3 mL of H_2O_2. The product was washed several times with HCl and DI water, followed by sonication and centrifugation to obtain a stable ~10 mg·mL^{-1} GO aqueous suspension.

Synthesis of reduced graphene oxide (rGO). The rGO was prepared by diluting the GO suspension to 1 mg·mL^{-1}, adding 35 mL into 50 mL Teflon-lined hydrothermal reactors, and heating it to 180 °C for 12 h. The resulting rGO foam was washed with DI water and freeze-dried, as described previously [6].

3.2. Adsorption experiments

Standard mercury (II) cation solutions. A 1000 mg·L^{-1} solution of Hg^{2+} cations was prepared by dissolving 854 mg of $Hg(NO_3)_2{\cdot}H_2O$ (> 98 %, Thermo Scientific) in DI water with the help of concentrated HNO_3, to a final volume of 500 mL, with the assumption that 1 mg·L^{-1} ≈ 1 mg·kg^{-1} for DI water. Other concentrations of mercury solutions were achieved by appropriate dilutions with DI water, and the pH was adjusted using 50 mM HNO_3 and NaOH solutions.

Batch adsorption isotherm and kinetics. The adsorption isotherm studies were conducted using an rGO dose of 0.5 g·L^{-1} (3 mg of rGO in 6 mL of solution) and a range of initial Hg^{2+} ion concentrations of C_0 = 50, 100, 200, 300, 400, 600, 800, and 1000 mg·L^{-1}. The pH was adjusted to 3 using drops of 50 mM NaOH and HNO_3 solutions. The glass vials were kept inside a thermal bath with a controlled temperature of 298 K, and the mixture was vigorously stirred overnight. After the equilibrium was reached, the solutions were collected with syringes and filtered through PVdF filters (Acrodisc® 0.45 μm, 25 mm Ø) for concentration analysis using calibrated X-ray fluorescence (XRF).

The kinetics study was performed using a 300 mg·g^{-1} solution of Hg^{2+} cations with an adjusted pH of 3. The rGO was added in a dose of 0.5 g·L^{-1} and vigorously stirred to ensure the immediate dispersion of the whole powder. Solution samples were collected with syringes after certain time intervals (from 0.5 to 120 min), filtered through PVdF filters, and the concentration was measured using XRF.

3.2.1. XAS experiments

Hg L_3-edge XAS data collection was performed at the CLEASS beamline of the ALBA synchrotron (Barcelona, Spain). *Ca.* 2 mg of the sample was loaded inside the PTFE tube with an inner diameter of 1.6 mm (1/16") and flushed using a syringe pump with the DI water at 2 mL·min^{-1}, ensuring the sample was completely free of air bubbles. Then, the solution of 300 mg·L^{-1} Hg at pH = 3 was introduced at 1 mL·min^{-1} with continuous measurement of XAS spectra in transmission mode using ionization chambers. The beam was focused down to 0.3 × 0.2 mm and aligned with the sample. Si (111) monochromator was operated in continuous scanning mode, resulting in 1 spectrum every 3 min. The obtained dataset was processed and analyzed on a self-written Python code using the Larch and PyFitit libraries [15,16].

3.2.2. QCM-D flow-cell experiments

Electrode Preparation. A 5 MHz QCM quartz crystal covered with a 5 mm diameter gold electrode was used as a support for the adsorption

experiments. The gold was initially coated with an indium tin oxide (ITO) layer followed by 100 nm graphitic carbon deposition to avoid undesired interactions with the mercury in solution. The rGO powder was dispersed at 5 $mg{\cdot}mL^{-1}$ in N-methyl-2-pyrrolidone (NMP), and the appropriate volume was drop-cast at the surface of the electrode to obtain a final mass loading of around 30 $\mu g{\cdot}cm^{-2}$.

Flow-cell. A peristaltic pump was used to keep the solution flux at 0.1 $mL{\cdot}min^{-1}$ to avoid turbulent measurements, and the temperature of the system was kept constant at 25 °C using a modular control. Initially, DI water was fluxed to remove any bubbles from the capillaries until the system and frequencies measured were stable. Milli-Q water was then fluxed for 15 min, followed by a 50 $mg{\cdot}L^{-1}$ Hg^{2+} ions solution at pH 3 for 90 min, and finally washed again using Milli-Q water.

4. Conclusions

Through combining microfluidic *in situ* XAS and EQCM-D, we demonstrate how a more comprehensive understanding of the adsorption dynamics and species involved in the adsorption of Hg^{2+} cations by rGO can be obtained. The batch isotherm and kinetics studies showed clear adsorption stages, where initially, the fast interactions with the oxygenated functional groups at the surface of the rGO, by chemisorption, occur, resulting in a high rate of mercury uptake. Subsequently, the predominant mechanism is based on electrostatic interactions with the π-electrons of the graphene structure of rGO. Finally, all thermodynamically available sites are occupied and equilibrium reached.

The EQCM-D data provide the mass changes and viscoelastic properties of the adsorbent layer under dynamic flow conditions. The significant frequency shifts observed upon the introduction of Hg^{2+} ions to the rGO-coated electrode confirm the effectiveness of the adsorption process. The *in situ* XAS offers real-time tracking of the local atomic and electronic changes around mercury ions during adsorption, and the evolution of the mercury L_3-edge spectra indicates a transition from a disordered to a more defined coordination environment, reflecting the progressive electrostatic interaction of Hg^{2+} ions with the rGO surface.

We identified two distinct mercury species, which can be correlated with the structural organization of adsorbed mercury cations with the rGO functional groups and, finally, the carbon surface of rGO. Initially, the chemisorbed species rapidly occupy the available sites, followed by a modest contribution of electrostatically adsorbed cations. The latter increases its adsorption rate as the chemisorption sites get saturated, and finally, the chemisorbed species are released in acidic flow conditions in exchange for H_3O^+ cations in solution.

The integration of microfluidic systems provided a detailed temporal and structural resolution of the adsorption events, allowing the formulation of potential mechanisms of interaction between the heavy metal ions and the rGO-based adsorbent. This study not only confirms rGO as an effective adsorbent for mercury ions but also provides new mechanistic insight into the adsorption process, using a simple and reproducible flow process. Moreover, this unique study coupling different *operando* techniques opens the way for more in-depth investigations of adsorption processes in flux of different kinds of materials, including rGO and many others currently emphasized in literature data, such as activated carbon and MXenes.

CRediT authorship contribution statement

Thierry Brousse: Writing – review & editing, Supervision, Project administration, Conceptualization. **Björn Wickman:** Supervision, Resources. **Patrik Johansson:** Writing – review & editing, Validation. **Camille Douard:** Methodology, Investigation. **Olivier Crosnier:** Writing – review & editing, Supervision. **Aram L. Bugaev:** Writing – review & editing, Formal analysis, Conceptualization. **Alina Skorynina:** Resources, Methodology, Investigation, Data curation. **Marcelo A. Andrade:** Writing – original draft, Visualization, Methodology, Investigation, Formal analysis.

Declaration of Competing Interest

The authors declare the following financial interests/personal relationships which may be considered as potential competing interests: Marcelo Amaro de Andrade reports financial support was provided by European Union's Horizon 2020 research and innovation program under the Marie Sklodowska-Curie Actions COFUND (Grant Agreement 945357). Patrik Johansson reports financial support was provided by Swedish Research Council (VR) Distinguished Professor grant Next Generation Batteries (2021–00613). Marcelo Amaro de Andrade reports financial support was provided by ReMade ARI project, part of the Horizon Europe call HORIZON-INFRA-2021-SERV-01 under grant agreement number 101058414. Aram L. Bugaev reports financial support was provided by Swiss National Science Foundation (SNSF) Starting Grant No. TMSGI2_226131. Thierry Brousse reports financial support was provided by Labex STORE-EX (ANR-10-LABX-76–01). If there are other authors, they declare that they have no known competing financial interests or personal relationships that could have appeared to influence the work reported in this paper.

Acknowledgements

As a part of the DESTINY Ph.D. program, this publication is acknowledged by funding from the European Union's Horizon2020 Research and Innovation Program under the Marie Skłodowska-Curie Actions COFUND (Grant Agreement #945357) and Conseil Régional des Pays de la Loire (Trajectoire Europe). The authors are also grateful for the financial support from the Swedish Research Council (VR) Distinguished Professor grant 'Next Generation Batteries' (#2021-00613). The authors would like to acknowledge the support of colleagues Niels Rieger, Isak Almyren, and Vera Roth.

Part of the ReMade@ARI project, funded by the European Union as part of the Horizon Europe call HORIZON-INFRA-2021-SERV-01 under grant agreement number 101058414 and co-funded by UK Research and Innovation (UKRI) under the UK government's Horizon Europe funding guarantee (grant number 10039728) and by the Swiss State Secretariat for Education, Research and Innovation (SERI) under contract number 22.00187. Views and opinions expressed are, however, those of the author(s) only and do not necessarily reflect those of the European Union, the UK Science and Technology Facilities Council, or the Swiss State Secretariat for Education, Research and Innovation (SERI). Neither the European Union nor the granting authorities can be held responsible for them.

The authors also acknowledge the funding of the Swiss National Science Foundation (SNSF) Starting Grant No. TMSGI2_226131.

Appendix A. Supporting information

Supplementary data associated with this article can be found in the online version at doi:10.1016/j.jece.2025.118680.

Data availability

Data will be made available on request.

References

[1] M.C. Henriques, S. Loureiro, M. Fardilha, M.T. Herdeiro, Exposure to Mercury and human reproductive health: a systematic review, Reprod. Toxicol. 85 (2019) 93–103.
[2] N.A.A. Qasem, R.H. Mohammed, D.U. Lawal, Removal of heavy metal ions from wastewater: a comprehensive and critical review, npj Clean. Water 4 (2021).
[3] P. Liu, C.J. Ptacek, D.W. Blowes, R.C. Landis, Mechanisms of Mercury removal by biochars produced from different feedstocks determined using X-ray absorption spectroscopy, J. Hazard. Mater. 308 (2016) 233–242.
[4] T. Tene, et al., Removal of Mercury(II) from aqueous solution by partially reduced graphene oxide, Sci. Rep. 12 (2022) 1–12.

[5] A. Barra, et al., Reduced graphene oxide foams modified with caffeic acid for water decontamination: capture and safe storage of Hg2, J. Environ. Chem. Eng. 12 (2024) 114120.
[6] M.A. Andrade, O. Crosnier, P. Johansson, T. Brousse, Energy from garbage: recycling heavy Metal-Containing wastewater adsorbents for energy storage, Adv. Energy Sustain. Res. (2024) **2400195.**
[7] T. Moragues, et al., Droplet-Based microfluidics reveals insights into cross-coupling mechanisms over Single-Atom heterogeneous catalysts, Angew. Chem. Int. Ed. 63 (2024) 1–6.
[8] A.V. Dobrovolskaya, et al., High-Quality in situ X-ray absorption spectroscopy monitoring of the palladium nucleation inside the 3D printed microfluidic chip, J. Phys. Chem. C 127 (2023) 20727–20733.
[9] A.M. Nightingale, A.D. Beaton, M.C. Mowlem, Trends in microfluidic systems for in situ chemical analysis of natural waters, Sens. Actuators B Chem. 221 (2015) 1398–1405.
[10] J. Li, et al., In situ sensors for flow reactors-a review, React. Chem. Eng. 6 (2021) 1497–1507.
[11] N. Convery, N. Gadegaard, 30 years of microfluidics, Micro Nano Eng. 2 (2019) 76–91.
[12] D.L. Sparks, in: D.L.B.T.-E.S.C. Sparks (Ed.), second ed.Sorption Phenomena on Soils, 5, Academic Press, 2003, pp. 133–186, https://doi.org/10.1016/B978-012656446-4/50005-0.
[13] L. Largitte, R. Pasquier, A review of the kinetics adsorption models and their application to the adsorption of lead by an activated carbon, Chem. Eng. Res. Des. 109 (2016) 495–504.
[14] V. Migliorati, M. Busato, P. D'Angelo, Solvation structure of the Hg(NO3)2 and Hg(TfO)2 salts in dilute aqueous and methanol solutions: an insight into the Hg2+ coordination chemistry, J. Mol. Liq. 363 (2022) 119801.
[15] M. Newville, Larch: an analysis package for XAFS and related spectroscopies, J. Phys. Conf. Ser. 430 (2013) 12007.
[16] A. Martini, et al., PyFitit: the software for quantitative analysis of XANES spectra using machine-learning algorithms, Comput. Phys. Commun. 250 (2020) 107064.